Supplementary Material for "Electrospray film deposition for solvent-elimination infrared spectroscopy"

Andrea Arangio, Christophe Delval[†], Giulia Ruggeri[‡],
Nikunj Dudani, Amir Yazdani, Satoshi Takahama

ENAC/IIE Swiss Federal Institute of Technology Lausanne, Lausanne, Switzerland

[†]now at European Patent Office, The Hague, Netherlands

[‡]now at World Health Organization, Geneva, Switzerland

Contents

S1 Calibration equation

In ATR-FTIR, the deposited film can be probed multiple times with evanescent waves generated from each reflection at the interface between IRE and the sample. The resulting reflectance $R = (1 - \alpha d_e)^N$ for N reflections through a sample is a function of its linear decadic absorption coefficient α,[1] and the effective thickness d_e. A mathematical approximation can be invoked to obtain a corollary to the Lambert law under conditions of weak absorption[2–4] ($\alpha d_e \ll 1$), where the absorbance A derived from the attenuation of radiation through a homogeneous medium is proportional to each of these variables:

$$A = -\log_{10} R \approx N \alpha d_e \ . \tag{S1}$$

d_e characterizes the equivalent path length through the sample that gives the same extinction by transmission measurements, and is approximated as:[2,5]

$$d_e = \frac{n_{21}}{\cos\theta}\int_{z=0}^{d} E^2 dz \quad \text{where} \quad E = E_0 \exp\left(-\frac{z}{d_p}\right) \ . \tag{S2}$$

$n_{21} = n_2/n_1$ is the ratio of the real parts of refractive indices of sample medium (n_2) to IRE (n_1), θ is the incident angle, E^2 is the electric field intensity, E_0 is the amplitude of the field at the IRE-sample interface, d_p is the penetration depth, and z is the distance outward from the surface of the IRE. The electric field is integrated from the surface ($z = 0$) to the sample thickness d. d_p is the e-folding distance (reciprocal of the exponential decay constant) for the evanescent wave and depends on the wavelength $\lambda_1 = \lambda/n_1$ in the IRE:[6]

$$d_p = \frac{\lambda_1}{2\pi\left(\sin^2\theta - n_{21}^2\right)^{1/2}} \ . \tag{S3}$$

In the limit of thick samples (semi-infinite medium, $d \gg d_p$, where the evanescent field E sufficiently decays inside the sample), the integral in Eq. S2 approaches $E_0^2 d_p/2$; prompting an empirical "correction" for ATR spectra to adjust for wavelength dependence (Eq. S3) in cases where comparison against transmission spectra are desired. The thin film approximation can be applied at the opposite extreme when $d \ll d_p$, where the electric field can be treated as a constant $E \approx E_0$.[6] The integral in Eq. S2 then approaches $E_0^2 d$, and the effective penetration depth is directly proportional to the physical thickness of the sample.

For substances in a mixture, the dependence of absorption on concentration c is described by corollary to Beer's law for transmission analysis, typically expressed as a relation through the linear absorption coefficient and molar absorption coefficient ε: $\alpha = \varepsilon c$. The analyte concentration multiplied by the film thickness $c \cdot d$ corresponds to an areal density m/a_N,[7] leading to a linear relation between A and deposited mass m for analyte i:

$$\begin{gathered} A = \sum_i \varepsilon_i' m_i \\ \text{where} \quad \varepsilon_i' = \left(\frac{N}{a_N \cos\theta}\right)\left(n_{21}E_0^2\right)\left(\frac{\varepsilon_i}{M_i}\right) \ . \end{gathered} \tag{S4}$$

The linear absorption coefficient, molar absorption coefficient, and refractive index (k)are related by:[7,8]

$$\varepsilon_i \rho_i / M_i = \alpha_i = 4\pi k_i \tilde{\nu} \log_{10} e \ . \tag{S5}$$

$\tilde{\nu}$ is the wavenumber and ρ is the mass density.

S2 Area coverage

In this section, we provide a mathematical argument that Eq. 4 with N/a_N fixed by the IRE geometry applies even for partial sample coverage along the dimension of beam propagation. The Lambert law for a thin film analyzed by ATR-FTIR is given by:

$$A = N\alpha d_e = N\alpha \frac{n_{21}E_0^2}{\cos\theta} d$$

Consider the placement of a pure substance with volumetric mass density ρ and molar mass M with complete coverage along IRE width W perpendicular to beam. Let the IRE area through which N^* reflections ($N^* = 10$

for our configuration) nominally pass be defined as $a_{N^*} = W \times L$. In a scenario where mass m^* covers the IRE completely, $m^* = \rho W L d^*$ and $N = N^*$. The apparent absorbance is given by

$$A^* = N^* \frac{n_{21} E_0^2}{\cos\theta} \alpha d^* = N^* \frac{n_{21} E_0^2}{\cos\theta} \alpha \frac{m^*}{\rho W L} = \left(N^* \frac{n_{21} E_0^2}{\cos\theta} \frac{\alpha}{\rho\, a_{N^*}} \right) m^* \ .$$

For incomplete lengthwise-IRE coverage of the same mass $m^* = \rho W \ell d$, the film is deposited such that $\ell \leq L$ (area coverage is $W \times \ell$), $d \geq d^*$ (film is thicker), and approximately $N = N^* \ell / L$ reflections pass through the sample. Since $N^*/WL \approx N/W\ell$, the apparent absorbance is remains constant ($A = A^*$) for the same mass loading as long as the thin-film approximation is not violated:

$$A = N \frac{n_{21} E_0^2}{\cos\theta} \alpha d = N^* \frac{\ell}{L} \frac{n_{21} E_0^2}{\cos\theta} \alpha \frac{m^*}{\rho W \ell} = \left(N^* \frac{n_{21} E_0^2}{\cos\theta} \frac{\alpha}{\rho\, a_{N^*}} \right) m^* \ .$$

This conclusion can be extended in a straightforward manner to the Beer-Lambert law by incorporating the concentration dependence on α.

S3 Single cone-jet electrospray theory

In the cone-jet mode, the cone breaks up at the tip, ejecting droplets for which the size distribution depends on the flow rate and the electrical conductivity of the purged solution.[9] Theoretically, the first droplet ejected from the cone-jet break up plays a central rule as its charge density determines the propagation speed of the spray and ultimately, the evaporation efficiency.[10] The radius of the first droplet R_e can be estimated[11] from the geometry of the cone and related parameters that affect its shape such as the flow rate Q, the ratio between the applied voltage V_a and the onset voltage V_o, together with the solution density ρ:

$$r_e = \left(\frac{\rho Q^2}{4\pi^2 \tan\left(\frac{\pi}{2} - \phi_T\right) \left[\left(\frac{V_a}{V_o}\right)^2 - 1 \right]} \right)^{1/3} \tag{S6}$$

ϕ_T is the characteristic Taylor angle (49.3°). Typically, the solvent density is used in place of the solution density ($\rho \approx \rho_s$). The charged droplet moves towards the grounded counter electrode dragged by electrostatic forces while shrinking due to solvent evaporation. The shrinkage causes the charge density to increase drastically and above a critical value q_R, the surface tension is not strong enough to counterbalance the Coulomb repulsion and the droplet bursts forming daughter droplets. The critical charge density q_R at which the disintegration takes place is called the Rayleigh limit and it is given by the following equation[12]:

$$q_R = \left[8\pi^2 \epsilon_0 \gamma_s (2r_e)^3 \right]^{1/2} \tag{S7}$$

The same process takes place also for the daughter droplets in which disintegration leads to the complete separation of solute molecules from the solvent and their deposition on the substrate. If the shrinkage process is limited only by evaporation (a valid approximation for small droplets), the time Δt between the emission of the first droplet and the subsequent disintegration is critical for an effective solvent separation; Δt is function of solvent vapor pressure P_s and temperature T[10]:

$$\Delta t = -\left(\frac{4\rho R T}{\alpha_g v P_s M_s} \right) \Delta r_e \tag{S8}$$

Δr_e is the difference between the initial droplet radius (Eq. S6) and droplet radius at disintegration (Eq. S7). R is the gas constant, M_s is the molar mass of the solvent, α_g is the gas accommodation coefficient, and v is the thermal velocity of the molecules in the gas phase. Depending on experimental conditions, the first fission occurs in the microsecond scale and later fissions at shorter intervals[10]. Δt can be used as a reference parameter to estimate the solute-to-solvent separation conditions when different solvents are compared.

S4 ES-ATR-FTIR device

Figure S1 shows the apparatus developed and used in this work. The voltage applied to the needle is controlled by a motherboard (USB X Series 128 channel - National Instruments) which inputs a voltage between 0 and 10 V to a voltage amplifier (10A12 - UltraVolt, Inc.). The needle position is varied along the long direction of the crystal by a motorized stage (MTS50/M-Z8 - 50mm - Thorlabs, Inc.) anchored on an XYZ stage (PT3 - 25 mm, Thorlabs, Inc.) used for fine vertical and plane positioning. The solution is injected to the needle by means of a stepper motor syringe pump. The instrumentation is kept in a purged chamber.

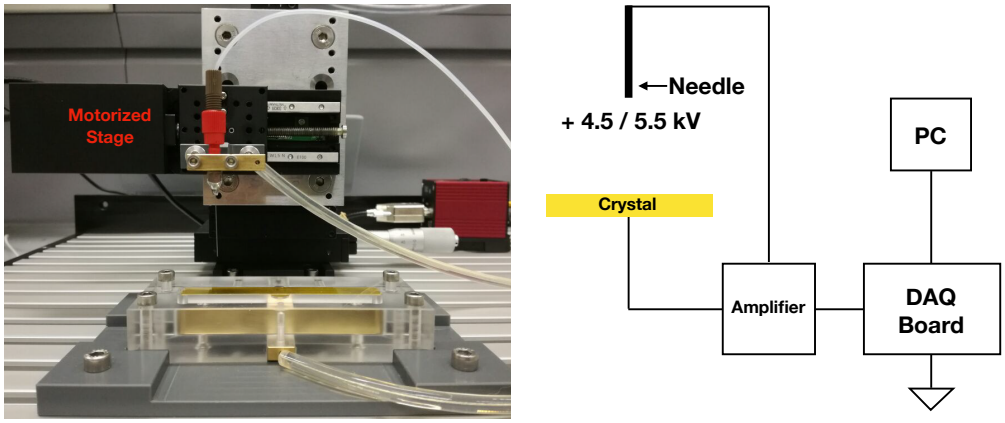

Figure S1: Photograph and diagram of the electrospray apparatus.

S5 Particle morphology

In this section, we characterize the influence of film morphology (i.e., particle formation) on the ATR absorbance spectrum. We compare two scenarios:

- Homogeneous film of thickness d
- Packed monolayer of monodisperse spheres with height $2R$

For a monolayer comprised of monodisperse spheres, let us assume an optimal compact (hexagonal) circle packing deposition. In two dimensions, the packing density η_h is:

$$\eta_h = \frac{\pi\sqrt{3}}{6} \approx 0.91$$

Let the areal density η_R scale with vertical distance z according to the projected area of a single sphere:

$$\eta_R(z) = \eta_h f_R(z) \quad \text{where} \quad f_R(z) = \frac{\pi[R^2 - (R-z)^2]}{\pi R^2} = \left[1 - \frac{(R-z)^2}{R^2}\right] .$$

A substance deposited as a packed monolayer of spheres would have a height $2R = 3d/2\eta_h$ ($\approx 1.7d$) greater than the same mass deposited over a homogeneous film of height d. This result can be obtained by mass

balance (with mass density ρ):

$$\int_0^d \rho dz = \int_0^{2R} \rho\, \eta_R(z) dz$$
$$\rho\, d = \rho\, \eta_h \int_0^{2R} \left[1 - \frac{(R-z)^2}{R^2}\right] dz$$
$$d = \frac{4}{3}\eta_h R \;\; (\approx 1.2R) \tag{S9}$$

The electric field of the evanescent wave that diffuse in the sample decays as a function of z and $E(z)$ is given by Eqs. S2 and S3. In the thin-film approximation with film thickness d,

$$\lim_{d\to 0} \int_0^d E_0^2 \exp\left(-2z/d_p\right) dz \to E_0^2 d\ .$$

The apparent absorbance of a homogeneous film and packed sphere monolayer relative to that for which the thin-film appoximation applies is given by:

$$\begin{aligned} &\text{Homogeneous film} && \frac{\int_0^d \exp\left(-2z/d_p\right)\, dz}{d} \\ &\text{Packed sphere monolayer} && \frac{\int_0^{2R=3d/2\eta_h} \exp\left(-2z/d_p\right) \eta_R(z)\, dz}{d}\ . \end{aligned} \tag{S10}$$

Calculations are shown in Figure S2.

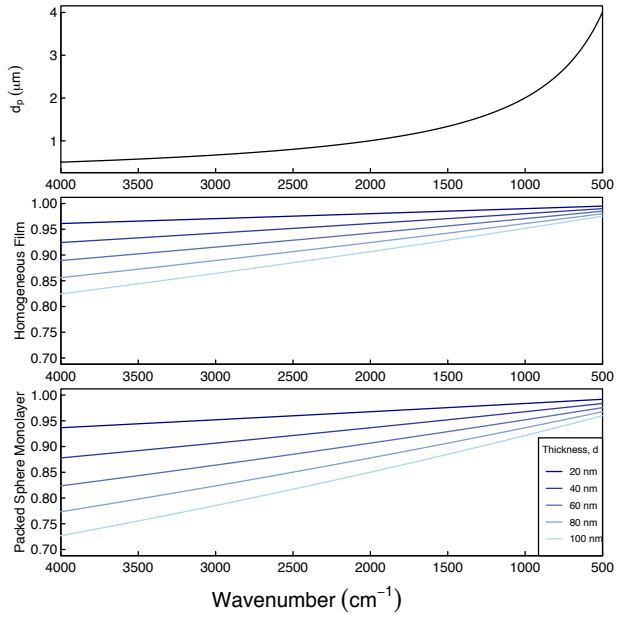

Figure S2: Calculated ratios of expected absorbance relative to wavelength-independent absorbance. Parameters used for calculations: $\theta = 45°$, $n_1 = 2.4$ (ZnSe), $n_2 = 1.5$.

The wavenumber-dependence and= magnitude of discrepancy between transmission-mode and electrosprayed ammonium nitrate spectra suggests that the difference could be due to particle deposition in the ES. Therefore, Eq. S10 is used together with Eq. S9 to estimate an effective particle diameter ($2R$) for electrosprayed

ammonium nitrate by an iterative search of R that leads to the observed magnitude of discrepancy with the transmission-mode spectra. This calculation is repeated for masses of ammonium nitrate accumulated on the IRE by stacking experiments (Figure S3). The analysis indicates that larger particles result from increases in the mass deposition. Even below 5 µg of loading, the particle size is estimated to be greater than 100 nm, with particles generated upon deposition of about 10 µg have estimated diameters of about 200 nm.

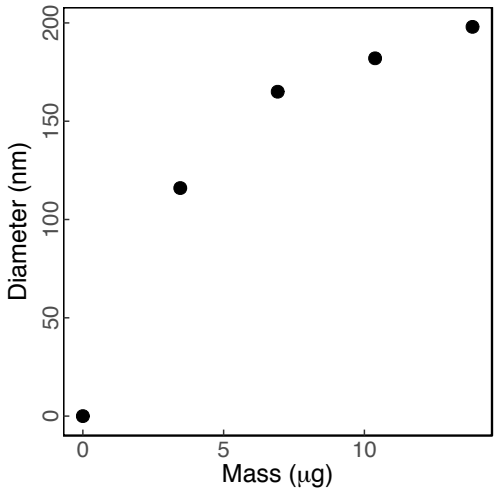

Figure S3: Estimated equivalent diameter of ammonium nitrate particles deposited with electrospray.

More generally, the penetration depth for intermediate cases between packed sphere monolayer and thin film can be written with an arbitrary packing density η_0 (e.g., square packing) in place of η_h. In the present case, n_2 was assumed constant for all cases, but porosity (density) of the substance will affect its value according to effective medium theory. Furthermore, these equations are not valid beyond the point that the length scale of heterogeneities (either $2R$ or pores of air) approach IR wavelengths, as this invalidates the possibility to consider the packed monolayer as a film with a single, refractive index by the effective medium approximation.

S6 Limit of detection

The limit of detection (LOD) was experimentally evaluated by depositing cumulatively 150 ng of docosanol by spraying 100 µL of a solution containing 1.5 µg mL^{-1}. Spectra were recorded using a liquid nitrogen cooled MCT detector. The calibration curve is reported in Figure S4 where the line in blue is the resulting linear regression from which the LOD is calculated as:

$$LOD = \frac{3 s_{Y|x}}{b} \text{ where } s_{Y|x} = \sqrt{\frac{\sum (\hat{y}_i - y_i)^2}{n-2}} \ .$$

b is the slope of the regression line and $s_{Y|x}$ is the mean squared error of calibration calculated from the number of samples n, and difference between observed (y_i) and fitted ($\hat{y}_i$) values. The resulting LOD is 48 ng.

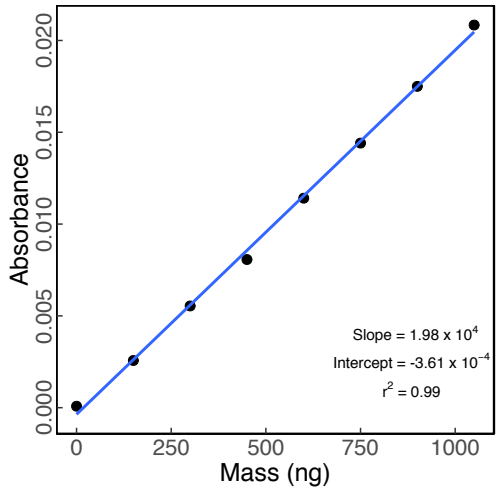

Figure S4: Calibration curve for docosanol ($\nu(-\mathrm{CH}) = 2900\ \mathrm{cm}^{-1}$) in the submicrogram loading range 150 – 1050 ng. Spectra were recorded using a liquid nitrogen cooled MCT detector.

S7 Experimental details - Test set

In the following section, experimental details are given on the test set for both docosanol and ammonium sulfate in Table S1. Additionally, a mixture spectrum of docosanol and ammonium sulfate from the test set is shown together with a spectrum reconstructed from its pure-component contributions (Figure S5).

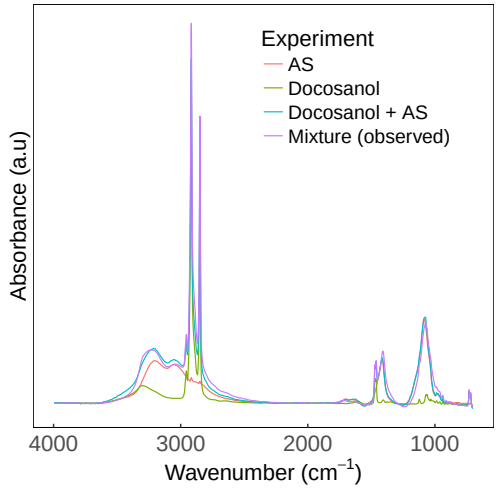

Figure S5: Spectra of pure docosanol (green) and ammonium sulfate (AS in red) from the calibration set, and a mixture spectrum from the test set (violet). Calibration sample spectra of docosanol and ammonium spectra (15.2 and 10.5 µg of loading, respectively) were normalized to unit mass and scaled by the calibration coefficient to obtain equivalent mass loadings in the mixture sample. The sum of the two spectra is shown in blue.

Table S1: Depositions performed to obtain the test dataset for both docosanol and ammonium sulfate shown in Figure 5a and 5b. Mass loadings indicated with (*) refer to depositions performed from a mixture solution of docosanol and ammonium sulfate.

Compound	Mass loading [µg]	Solution concentration [µg/mL]	Volume [mL]	Repetitions
Docosanol	6.4	6.4	1.0	3
Docosanol	11.8	11.8	1.0	3
Docosanol	16.5	16.5	1.0	3
Docosanol	25.2	25.2	1.0	3
Docosanol	34.2	34.2	1.0	3
Docosanol	39.1	39.1	1.0	3
Docosanol	4.6*	15.2	0.3	1
Docosanol	7.6*	15.2	0.5	1
Docosanol	15.2*	15.2	1.0	1
Docosanol	22.9*	15.2	2.0	1
Amm. Sulf.	7.1	59.3	0.12	1
Amm. Sulf.	14.2	59.3	0.24	1
Amm. Sulf.	21.3	59.3	0.36	1
Amm. Sulf.	25.0	25.0	1.0	1
Amm. Sulf.	26.0	26.0	1.0	1
Amm. Sulf.	28.5	28.5	1.0	1
Amm. Sulf.	3.2*	10.6	0.3	1
Amm. Sulf.	5.3*	10.6	0.5	1
Amm. Sulf.	10.6*	10.6	1.0	1
Amm. Sulf.	15.9*	10.6	2.0	1

S8 Volatility

In this section, we provide calculations which show that cis-pinonic acid and docosanol are likely phase-separated after evaporation of methanol solvent, and estimates of vapor pressures that drive the evaporation for initial and final states.

S8.1 Miscibility

In order to understand a priori whether cis-pinonic acid and docosanol produce a homogeneous phase or they separate to form a film deposition with two phases, the Hansen Solubility Parameter (HSP) has been determined using the functional group contribution method.[13] We adapted the notation outlined by Ye et al.[14] in the following description. Within the Hansen solubility framework, the total solubility parameter $\delta_{t,i}$ determines the miscibility between two organic compounds. $\delta_{t,i}$ takes into account three types of intermolecular forces: dispersion forces ($\delta_{d,i}$), dipole-dipole interactions ($\delta_{p,i}$), and hydrogen bonding ($\delta_{hb,i}$). All contributions are combined according to the following equation:

$$\delta_{t,i}^2 = \delta_{d,i}^2 + \delta_{p,i}^2 + \delta_{hb,i}^2 \ .$$

For a particular fucntional group k in a molecule i, its contribution each intermolecular force to the solubility can be calculated from the compiled "molar attraction constant", $F_{d,k}$, $F_{p,k}$, and $E_{hb,k}$[14] according the

following equations:

$$\delta_{d,i} = \sum_k \frac{c_k^i F_{d,k}}{V_k};\ \delta_{p,i} = \frac{\sqrt{\sum_k c_k^i F_{p,k}^2}}{V_k};\ \delta_{hb,i} = \sqrt{\sum_k \frac{c_k^i E_{hb,k}}{V_i}}$$

where c_k^i is the number of the functional group k in the molecule i and V_i is the molecular volume of the compound calculated as a sum of molecular volumes of all functional groups in the molecule. The $\delta_{t,i}$ gives a qualitative estimation of organic miscibility, but each contribution can be used to calculate the Gibbs free energy of the mixing using the Flory-Huggins equation.[15,16] For cis-pinonic acid (cpa) and docosanol (doc):

$$\Delta_{mix}G = \Delta_{mix}H - T\Delta_{mix}S = RT(n_{\text{cpa}} + mn_{\text{doc}})\chi\varphi_{\text{cpa}}\varphi_{\text{doc}} - T[-R(n_{\text{cpa}}\ln\varphi_{\text{cpa}} + n_{\text{doc}}\ln\varphi_{\text{doc}})]$$

where n_{cpa} and n_{doc} are the number of moles of cis-pinonic acid and docosanol respectively, R is the gas constant (8.2×10^{-5} $\text{m}^3\text{atm}\,\text{mol}^{-1}\text{K}^{-1}$), and T is the temperature in Kelvin. Additionally:

$$\varphi_{cpa} = \frac{n_{\text{cpa}}}{n_{\text{cpa}} + mn_{\text{doc}}};\ \varphi_{\text{doc}} = \frac{mn_{\text{doc}}}{n_{\text{cpa}} + mn_{\text{doc}}};\ \text{and}\ m = \frac{V_{\text{doc}}}{V_{\text{cpa}}}\ ,$$

and the parameter χ is the Flory-Huggins parameter defined as:

$$\chi = \frac{V_{\text{cpa}}}{RT}\left[(\delta_{d,\text{cpa}} - \delta_{d,\text{doc}})^2 + \frac{1}{4}(\delta_{p,\text{cpa}} - \delta_{p,\text{doc}})^2 + \frac{1}{4}(\delta_{hb,\text{cpa}} - \delta_{hb,\text{doc}})^2\right]\ .$$

In the experiments reported in this work, $n_{\text{cpa}} = 8.15 \times 10^{-8}$ mol, $n_{\text{doc}} = 4.61 \times 10^{-8}$ mol, and $T = 296.15$ K. The resulting Gibbs free energy of mixing is $\Delta_{mix}G = 2.4 \times 10^{-5}$ J, indicating slighlty unfavorable mixing conditions.

S8.2 Vapor pressure estimation

Considering concentrations at two extremes: that of the bulk solution and final deposited state, we calculate differences in equilibrium vapor pressure of the substances (Table S2) that drives the rate of mass transfer. The temperature dependencies are shown in Figure S6. Calculations are shown below.

Table S2: Thermodynamic properties. "soln" indicates bulk solution composition. x is the mole fraction and γ is the activity coefficient. p denotes the pressure for cis-pinonic acid (cpa) and K_p is the dissociation constant for ammonium nitrate (AN). [*] liquid mixture with docosanol is calculated for comparison.

		binary mixture			tertiary mixture		
	form	x	γ or γ^2	p or K_p	x	γ or γ^2	p or K_p
cpa	soln	3.3×10^{-6}	3.9	$1.3 \times 10^{-5} p^0_{\text{cpa}}$	3.3×10^{-6}	3.9	$1.3 \times 10^{-5} p^0_{\text{cpa}}$
	solute[*]			p^0_{cpa}	6.4×10^{-1}	1.4	$0.9\, p^0_{\text{cpa}}$
AN	soln	5.4×10^{-6}	4.3	$1.3 \times 10^{-10} K_{\text{AN(aq)}}$	NH_4^+=1.2×10^{-5} NO_3^-=5.4×10^{-6}	4.1	$2.7 \times 10^{-10} K_{\text{AN(aq)}}$
	solute			$K_{\text{AN(s)}}$			$K_{\text{AN(s)}}$

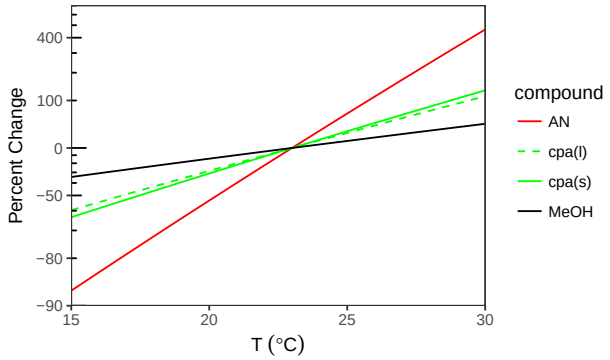

Figure S6: Percent change in vapor pressure with respect to 23 °C, which is the nominal temperature of current experiments. (Note logarithmic y-axis scale.) The nominal phase of pure cis-pinonic acid at room temperature is solid, but liquid-phase vapor pressures for cis-pinonic acid are also shown for reference as environmental organic compound mixtures can often be anticipated exist in non-solid phases.[17,18]

Organic compounds [cis-pinonic acid (cpa) and methanol (MeOH)]. The gas-particle partitioning process of cpa and methanol can be written as reversible reactions:

$$\begin{aligned} \mathrm{cpa}_{(\mathrm{s})} &\leftrightharpoons \mathrm{cpa}_{(\mathrm{g})} \\ \mathrm{cpa}_{(\mathrm{l})} &\leftrightharpoons \mathrm{cpa}_{(\mathrm{g})} \\ \mathrm{MeOH}_{(\mathrm{l})} &\leftrightharpoons \mathrm{MeOH}_{(\mathrm{g})} \end{aligned}$$

The phase state of cpa is solid at room temperature (23 °C in our experiments). As shown in the previous section, cpa is likely phase-separated from docosanol at these conditions. However, given the larger range of compounds with which cpa can be mixed in environmental solutions, we consider the vapor pressure of cpa in both the solid phase and vapor phase. Only the liquid phase for MeOH is considered. The equilibrium constants[19] K_i are equal to the pure component vapor pressures for solid or subcooled liquid (ideal solution reference):

$$\begin{aligned} K_{\mathrm{cpa(s)}} &= p^0_{\mathrm{cpa(s)}} \\ K_{i(\mathrm{l})} &= p^0_{i(\mathrm{l})} = \frac{p_i}{\gamma_i x_i} \ . \end{aligned}$$

x is the mole fraction and γ is the activity coefficient, and p^0 is the pure-component vapor pressure. Equilibrium vapor pressures are given as:

$$\begin{aligned} p_{\mathrm{cpa(s)}} &= K_{\mathrm{cpa(s)}} \\ p_{i(\mathrm{l})} &= K_{i(\mathrm{l})} \gamma_i x_i \ . \end{aligned}$$

$p^0_{\mathrm{cpa(l)}}(T = 296.15\,\mathrm{K}) = 1.1 \times 10^{-7}\,\mathrm{atm}$ is calculated with the group contribution model, SIMPOL.1[20]. $p^0_{\mathrm{cpa(s)}}(T = 296.15\,\mathrm{K}) = 0.39\, p^0_{\mathrm{cpa(l)}} = 4.3 \times 10^{-8}\,\mathrm{atm}$ is estimated from the following equations[21,22] and values in Table S3. Terms that should be considered more generally but not specifically relevant for cis-

pinonic acid are denoted in $\{\cdot\}$.

$$p^0_{\mathrm{cpa(s)}}(T) = p^0_{\mathrm{cpa(l)}}(T) \exp\left[\frac{\Delta_{fus}S^m_{\mathrm{cpa}}}{R}\left(1 - \frac{T_{m,\mathrm{cpa}}}{T}\right)\right]$$

$$\Delta_{fus}S^m_{\mathrm{cpa}} = \Delta_{fus}S_{\mathrm{aah}} + \Delta_{fus}S_{\mathrm{ring}} + \Delta_{fus}S_{\mathrm{corr}} + \Delta_{fus}S_{\mathrm{groups}}$$

$$\Delta_{fus}S_{\mathrm{aah}} = \sum_i n_i G_i + n_{\mathrm{CH_2}} C_{\mathrm{CH_2}} G_{\mathrm{CH_2}} \tag{S11}$$

$$\Delta_{fus}S_{\mathrm{ring}} = 33.4 + 3.7(n-3) \tag{S12}$$

$$\Delta_{fus}S_{\mathrm{corr}} = \sum_i n_i G_i + \{\mathrm{CH_2\ group\ terms}\} \tag{S13}$$

$$\Delta_{fus}S_{\mathrm{groups}} = \sum_i n_i C_i G_i + \{\mathrm{total\ substitution\ terms}\} \tag{S14}$$

The value of $\Delta_{fus}S_{\mathrm{cpa}}$ is calculated to be $52.4\,\mathrm{J\,mol^{-1}\,K^{-1}}$. The Clausius-Clapeyron equation[23] is used for estimating the change in vapor pressure ($T_0 = 296.15\,\mathrm{K}$):

$$p^0_{\mathrm{cpa(s)}}(T) = p^0_{\mathrm{cpa(s)}}(T_{m,\mathrm{cpa}}) \exp\left[-\frac{\Delta_{\mathrm{sub}}H^m_{\mathrm{cpa}}}{R}\left(\frac{1}{T} - \frac{1}{T_{m,\mathrm{cpa}}}\right)\right]$$

$$p^0_{i(\mathrm{l})}(T) = p^0_{i(\mathrm{l})}(T_0) \exp\left[-\frac{\Delta_{\mathrm{vap}}H^0_i}{R}\left(\frac{1}{T} - \frac{1}{T_0}\right)\right] .$$

The heat of sublimation is calculated as $\Delta_{sub}H^m_{\mathrm{cpa}} = \Delta_{fus}H^m_{\mathrm{cpa}} + \Delta_{vap}H^m_{\mathrm{cpa}}$ where $\Delta_{fus}H^m_{\mathrm{cpa}} = \Delta_{fus}S^m_{\mathrm{cpa}}T_{m,\mathrm{cpa}}$. $\Delta_{vap}H_{\mathrm{cpa}}$ is calculated by the SIMPOL.1 model and thermodynamic data is taken from the NIST Chemistry Webbook[24] for MeOH.

Table S3: Parameter values applicable for cpa taken from Chikos et al.[21] Units of G are $\mathrm{J\,mol^{-1}\,K^{-1}}$. $T_{m,\mathrm{cpa}} = 67.85\,^{\circ}\mathrm{C}$ for cpa.[25]

Eq.	Group	n	Parameters
(S11)	primary sp^3 (CH_3)	3	$G = 17.6$
	secondary sp^3 (CH_2)	2	$G = 7.1$, $C_{\mathrm{CH_2}} = 1$
	tertiary sp^3 (CH)	1	$G = -16.4$
(S12)	ring	1	none
(S13)	cyclic tertiary sp^3 (CH(R))	1	$G = -14.7$
	cyclic quarternary sp^3 ($C(R)_2$)	1	$G = -34.6$
(S14)	ketone (C=O)	1	$G = 4.6$
	carboxylic acid (COOH)	1	$G = 13.4$

Ammonium nitrate (AN). Gas-particle partitioning of solid or aqueous ammonium nitrate can be written:[26]

$$\mathrm{NH_4NO_{3(s)}} \leftrightharpoons \mathrm{NH_{3(g)}} + \mathrm{HNO_{3(g)}}$$

$$\mathrm{NH_{4\,(aq)}^{+}} + \mathrm{HNO_{3\,(aq)}^{-}} \leftrightharpoons \mathrm{NH_{3(g)}} + \mathrm{HNO_{3(g)}} .$$

For ammonium nitrate in water, the volatilization is controlled by the acid-base reaction involving ammonia and nitric acid. The equilibrium constants for these processes are given by:

$$K_{\mathrm{AN(s)}} = p_{\mathrm{NH_3}} p_{\mathrm{HNO_3}} = \exp\left(-\frac{\Delta_f G_{\mathrm{NH_3}} + \Delta_f G_{\mathrm{HNO_3}} - \Delta_f G_{\mathrm{NH_4NO_3}}}{RT}\right)$$

$$K_{\mathrm{AN(aq)}} = \frac{p_{\mathrm{NH_3}} p_{\mathrm{HNO_3}}}{\gamma^2_{\mathrm{NH_4NO_3}} x_{\mathrm{NH_3}} x_{\mathrm{HNO_3}}} = \exp\left(-\frac{\Delta_f G_{\mathrm{NH_3}} + \Delta_f G_{\mathrm{HNO_3}} - \Delta_f G_{\mathrm{NH_4^+}} - \Delta_f G_{\mathrm{NO_3^-}}}{RT}\right)$$

with $\gamma^2_{\mathrm{NH_4NO_3}}$ is the mean mixed activity coefficient and follows the ideal-dilute solution reference for solutes. The temperature dependence $\Delta_f G_i = \Delta_f G_i(T)$ is calculated by:

$$\Delta_f G_i(T) = T\left[\frac{\Delta_f G_i^0}{T_0} + \Delta_f H_i^0\left(\frac{1}{T} - \frac{1}{T_0}\right) + c_{p,i}\left(\ln\frac{T_0}{T} - \frac{T_0}{T} + 1\right)\right]$$

with values for $\Delta_f G_i^0, \Delta_f H_i^0, c_{p,i}$ correspond to $T_0 = 298.15\,\mathrm{K}$.[27] The dissociation constants $K_p = p_{\mathrm{NH_3}} p_{\mathrm{HNO_3}}$ are given by:

$$K_{p(\mathrm{s})} = K_{\mathrm{AN(s)}}$$
$$K_{p(\mathrm{aq})} = K_{\mathrm{AN(aq)}} \gamma^2_{\mathrm{NH_4NO_3}} x_{\mathrm{NH_3}} x_{\mathrm{HNO_3}}$$

We obtain $K_{\mathrm{AN(s)}}(T = 296.15\,\mathrm{K}) = 34.79\,\mathrm{ppb}^2$ and $K_{\mathrm{AN(aq)}}(T = 296.15\,\mathrm{K}) = 2.51\,\mathrm{ppb}^2$. While the reported relative humidity (RH) at which aqueous ammonium nitrate crystallizes can be as low as 0%,[28–30] Wu et al.[31] observed solid ammonium nitrate formation at approximately 10% RH. That water absorption bands are not detected in our spectra does not rule out the possibility that ammonium nitrate is not fully crystallized after deposition, we have assumed that the deposited ammonium nitrate is solid for the purposes of this comparison.

References

1. IUPAC. IUPAC compendium of chemical terminology: Gold book, 2009. URL http://goldbook.iupac.org. DOI: 10.1351/goldbook.
2. Kortüm G, Braun W and Herzog G. *Principles and Techniques of Diffuse-Reflectance Spectroscopy*, volume 2. 1963.
3. Milosevic M. *Internal reflection and ATR spectroscopy*. Chemical anaysis, John Wiley & Sons, Inc., 2012. ISBN 978-0-470-27832-1.
4. Woods DA and Bain CD. Total internal reflection spectroscopy for studying soft matter. *Soft Matter* 2014; 10(8): 1071. DOI:10.1039/c3sm52817k.
5. Wendlandt HG and Hecht WWM. *Reflectance Spectroscopy*. Interscience Publishers, 1966. ISBN 978-0-470-93363-3.
6. Harrick NJ. *Internal reflection spectroscopy*. Harrick Scientific Corp, 1967. ISBN 978-0-933946-13-2.
7. Adamson AW. *A Textbook of Physical Chemistry*. 2nd ed. Academic Press, 1979. ISBN 978-0-12-044262-1.
8. Ramer G and Lendl B. Attenuated total reflection Fourier transform infrared spectroscopy. In Meyers RA (ed.) *Encyclopedia of Analytical Chemistry*. John Wiley & Sons, Ltd, 2006. DOI:10.1002/9780470027318.a9287/abstract.

9. Chen DR, Pui DY and Kaufman SL. Electrospraying of conducting liquids for monodisperse aerosol generation in the 4 nm to 1.8 μm diameter range. *Journal of Aerosol Science* 1995; 26(6): 963–977. DOI:10.1016/0021-8502(95)00027-a.

10. Tang L and Kebarle P. Dependence of ion intensity in electrospray mass spectrometry on the concentration of the analytes in the electrosprayed solution. *Analytical Chemistry* 1993; 65(24): 3654–3668.

11. Wilm MS and Mann M. Electrospray and taylor-cone theory, dole's beam of macromolecules at last? *International Journal of Mass Spectrometry and Ion Processes* 1994; 136(2): 167–180.

12. Gomez A and Tang K. Charge and fission of droplets in electrostatic sprays. *Physics of Fluids* 1994; 6(1): 404–414. DOI:10.1063/1.868037.

13. Krevelen DWV. *Properties of Polymers: Their Correlation with Chemical Structure*. Elsevier Science Ltd, 1976. ISBN 0444414673.

14. Ye J, Gordon CA and Chan AWH. Enhancement in secondary organic aerosol formation in the presence of preexisting organic particle. *Environmental Science & Technology* 2016; 50(7): 3572–3579. DOI: 10.1021/acs.est.5b05512.

15. Flory PJ and Rehner J. Statistical mechanics of cross-linked polymer networks II. swelling. *The Journal of Chemical Physics* 1943; 11(11): 521–526. DOI:10.1063/1.1723792.

16. Blanks RF and Prausnitz JM. Thermodynamics of polymer solubility in polar and nonpolar systems. *Industrial & Engineering Chemistry Fundamentals* 1964; 3(1): 1–8. DOI:10.1021/i160009a001.

17. Marcolli C, Luo BP and Peter T. Mixing of the organic aerosol fractions: Liquids as the thermodynamically stable phases. *Journal of Physical Chemistry A* 2004; 108(12): 2216–2224. DOI:10.1021/jp036080l.

18. Koop T, Bookhold J, Shiraiwa M et al. Glass transition and phase state of organic compounds: dependency on molecular properties and implications for secondary organic aerosols in the atmosphere. *Physical Chemistry Chemical Physics* 2011; 13(43): 19238–19255. DOI:10.1039/c1cp22617g.

19. Denbigh K. *The Principles of Chemical Equilibrium*. Cambridge University Press, Cambridge, UK, 1981.

20. Pankow JF and Asher WE. Simpol.1: a simple group contribution method for predicting vapor pressures and enthalpies of vaporization of multifunctional organic compounds. *Atmospheric Chemistry and Physics* 2008; 8(10): 2773–2796. DOI:10.5194/acp-8-2773-2008.

21. Chickos JS, Acree WE and Liebman JF. Estimating solid–liquid phase change enthalpies and entropies. *Journal of Physical and Chemical Reference Data* 1999; 28(6): 1535–1673. DOI:10.1063/1.556045.

22. Lei YD, Chankalal R, Chan A et al. Supercooled liquid vapor pressures of the polycyclic aromatic hydrocarbons. *Journal of Chemical & Engineering Data* 2002; 47(4): 801–806. DOI:10.1021/je0155148.

23. Schwarzenbach RP, Gschwend PM and Imboden DM. *Environmental Organic Chemistry*. 2nd ed. John Wiley & Sons, 2002.

24. Thermodynamics Research Center M NIST Boulder Laboratories. Thermodynamics source database. In Linstrom P and Mallard W (eds.) *NIST Chemistry WebBook, NIST Standard Reference Database Number 69*. National Institute of Standards and Technology, 2018. DOI:10.18434/T4D303.

25. Bradley JC, Lang A and Williams A. Jean-Claude Bradley Double Plus Good (Highly Curated and Validated) Melting Point Dataset. Technical report, 2014. DOI:10.6084/m9.figshare.1031638.v1.

26. Seinfeld J and Pandis S. *Atmospheric Chemistry and Physics: From Air Pollution to Climate Change*. 3rd ed. New York, NY: John Wiley & Sons, 2016. ISBN 9781119221166.

27. Ansari AS and Pandis SN. Prediction of multicomponent inorganic atmospheric aerosol behavior. *Atmospheric Environment* 1999; 33(5): 745–757.

28. Richardson C and Hightower R. Evaporation of ammonium nitrate particles. *Atmospheric Environment (1967)* 1987; 21(4): 971 – 975. DOI:https://doi.org/10.1016/0004-6981(87)90092-8.

29. Lightstone JM, Onasch TB, Imre D et al. Deliquescence, efflorescence, and water activity in ammonium nitrate and mixed ammonium nitrate/succinic acid microparticles. *The Journal of Physical Chemistry A* 2000; 104(41): 9337–9346. DOI:10.1021/jp002137h.

30. Martin ST, Schlenker JC, Malinowski A et al. Crystallization of atmospheric sulfate-nitrate-ammonium particles. *Geophysical Research Letters* 2003; 30(21): 2102. DOI:10.1029/2003GL017930.

31. Wu HB, Chan MN and Chan CK. Ftir characterization of polymorphic transformation of ammonium nitrate. *Aerosol Science and Technology* 2007; 41(6): 581–588. DOI:10.1080/02786820701272038.